Material strategies for energy-efficient voltage-controlled magnetic tunnel junctions

Takayuki. Nozaki[1], Tomohiro Ichinose[1], Tatsuya Yamamoto[1], Jun Uzuhashi[2], Tomohiro Nozaki[1], Hiroyasu Nakayama[1], Atsushi Sugihara[1], Makoto Konoto[1], Kay Yakushiji[1], Tadakatsu Ohkubo[2] and Shinji Yuasa [1]*

1 National Institute of Advanced Industrial Science and Technology(AIST), Research Institute for Hybrid Functional Integration, Tsukuba, Ibaraki 305-8568, Japan

2 National Institute for Materials Science (NIMS), Research Center for Magnetic and Spintronic Materials, Tsukuba, Ibaraki 305-0047, Japan

*Email: nozaki-t@aist.go.jp

KEYWORDS

Voltage-controlled magnetic anisotropy, Interfacial perpendicular magnetic anisotropy,

Tunnel magnetoresistance, Magnetoresistive random access memory

ABSTRACT

The realization of spin manipulation using electric fields is anticipated to be a promising route toward future spintronic devices with ultra-low driving power as well as zero standby power, such as voltage-controlled (VC) - magnetoresistive random access memory (MRAM). Among various methods, the voltage-controlled magnetic anisotropy (VCMA) effect in magnetic tunnel junctions (MTJs) is regarded as a particularly effective approach for achieving electric-field-induced magnetization control. One of the most important technical challenges in VC-MRAM development is to achieve a large VCMA coefficient, which is essential for ensuring scalability and reliable information writing. This review discusses the fundamental aspects of the VCMA effect and outlines recent attempts to optimize material and device structures to improve the VCMA coefficient in both epitaxial and polycrystalline MTJs.

1. Introduction

The recent rapid proliferation of artificial intelligence (AI) and the internet of things (IoT) has led to a drastic increase in the power consumption of information technology (IT) infrastructures, including data centers and communication networks. In particular, AI technologies that involve advanced computational processes, such as deep learning, require vast computational resources. As a result, memory operations, such as storing model parameters and accessing intermediate data, consume a significant portion of the total energy, even exceeding the power required for computation itself. This issue becomes especially critical for edge AI technologies due to their strict power constraints. To enable real-time, intelligent processing at the edge without relying on constant cloud connectivity, the development of energy-efficient memory solutions is strongly required.

Among the various approaches to reducing the power consumption in memory processing for IT electronic devices, the adoption of nonvolatile working memory is considered one of the most effective solutions. Unlike conventional volatile memories such as DRAM and SRAM, nonvolatile memory can retain information even when the power is turned off, enabling a significant reduction in standby power consumption. While various types of nonvolatile memory based on different physical phenomena have been proposed, the development of magnetoresistive random access memory (MRAM) is gaining increasing importance as a promising candidate for ideal nonvolatile working memory due to its potential to achieve high operation speed (< 10 ns), excellent writing endurance (> 10^{12}) and a large capacity (> Gbit) all which can be achieved simultaneously[1]. One of the challenges in MRAM development, however, is to achieve a reduction in the information writing energy.

In MRAM, a magnetic tunnel junction (MTJ) is combined with a selection CMOS transistor as a 1-bit memory element. The MTJ consists of a layered structure in which an MgO tunneling barrier is sandwiched between two ferromagnetic metal electrodes, which are referred to as the free layer and the reference layer[2,3]. The device exhibits a tunneling magnetoresistance (TMR) effect, where the tunneling resistance changes according to the relative magnetization orientation of the two ferromagnetic layers. This enables electrical readout of magnetic information.

As of now, magnetization switching controlled by an electric current is used for writing information. In first-generation MRAM, called toggle-MRAM, an Oersted magnetic field generated by electric-current flowing through an external wiring was used. The toggle MRAM, while featuring high endurance as a key advantage, required a large writing power due to its indirect writing scheme and has also faced difficulties in achieving scalability. In contrast, the discovery of spin-transfer torque[4-7], a direct quantum mechanical effect that utilizes the angular momentum carried by a spin-polarized electric current, bought about a major technical breakthrough in achieving low-power magnetization manipulation and ensuring scalability. An extremely low writing energy of 45 fJ/bit has been achieved in an MgO double barrier structure employing a dual-reference-layer configuration[8]. This value is remarkably low, even comparable to the charging energy of a DRAM cell; however, it is still more than an order of magnitude higher than that of SRAM (< a few fJ/bit). This is because, in any current-driven operation, unwanted energy loss due to Ohmic dissipation is inevitable. From this perspective, the realization of electric-field-induced spin control[9], which can achieve writing energy as low as a few fJ/bit, has long been desired (Fig. 1).

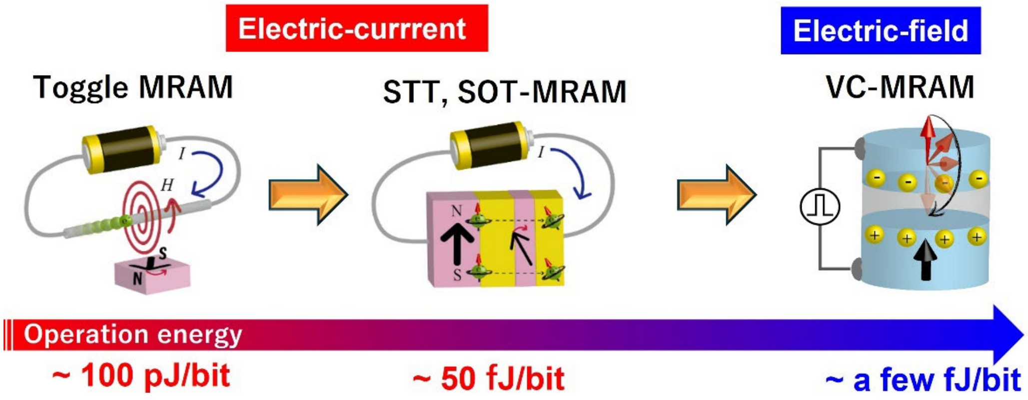

Figure 1 Trends in MRAM writing techniques and their energy consumption.

Following pioneering studies on the control of the Curie temperature via electric-field-induced carrier modulation in ferromagnetic semiconductors[10], various approaches to the electric-field control of spin have been proposed, including inverse magnetostrictive effects[11], control of exchange bias through the magnetoelectric effect[12,13], magnetic phase transition driven by electric-field-induced phase transition[14], induction of single phase multiferroics[15,16] and the engineering of two-phase multiferroic heterostructures[17]. Notable attention has been drawn to the voltage-controlled magnetic anisotropy (VCMA) effect[18,19] due to its high potential for practical application.

In this paper, we review the material development of voltage-controlled MTJs, with a particular focus on their application to voltage-controlled (VC)-MRAM[20-24]. In section 2, we first provide an overview of the fundamental characteristics and physical origin of the VCMA effect, as well as the mechanism of magnetization switching utilizing VCMA-induced precessional dynamics. Section 3 introduces various attempts to obtain a guideline for materials design aimed at improving the VCMA effect, with a particular focus on epitaxial junctions. In section 4, we present recent efforts to enhance the VCMA properties in polycrystalline MTJs prepared by sputtering for mass-production, especially highlighting the effective use of cryogenic temperature deposition processes.

2. Overview of the VCMA effect and voltage-induced dynamic switching

The VCMA effect was first demonstrated in FePt(Pd) thin films immersed in a liquid electrolyte[18], and was later applied to all-solid-state devices using MgO insulating layers[19], eventually leading to its application in an MTJ structure[25]. Figure 2(b) shows an example of the effect of bias voltage on the polar-MOKE hysteresis curves of an ultrathin CoFe layer in a multilayer structure consisting of Au buffer/CoFe (0.58 nm)/MgO/polyimide/ITO[26]. The sign of the bias voltage is defined with respect to the top electrode (see Fig. 2(a)).

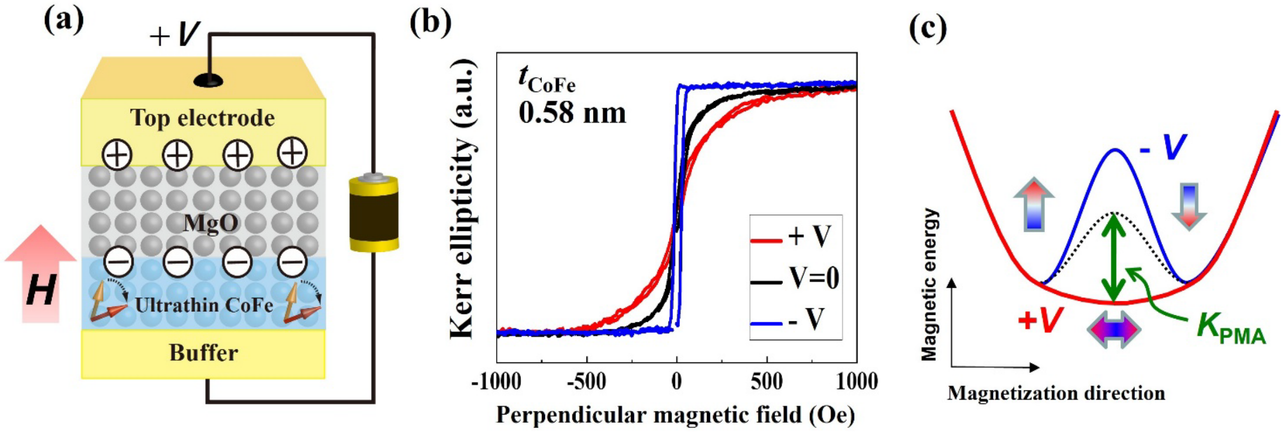

Figure 2 (a) Conceptual schematic of the VCMA effect, (b) bias voltage effect on polar-MOKE hysteresis curves observed in an Au/CoFe/MgO/Polyimide/ITO junction, and (c) schematic illustration of the change in magnetic energy profile induced by the VCMA effect. The magnetic energy barrier associated with PMA can be modulated by a bias voltage.

Under positive (negative) bias voltage, which induces electron accumulation (depletion) at the CoFe/MgO interface, the perpendicular magnetic anisotropy (PMA) is reduced (increased). This indicates that the height of the magnetic energy potential associated with perpendicular uniaxial magnetic anisotropy is being controlled by the applied electric field (Fig. 2(c)).

For the quantitative evaluation of the efficiency of the VCMA effect, an orthogonally magnetized MTJ is often used[27,28]. Figure 3(a) presents a typical example of the bias voltage dependence of TMR curves measured under an in-plane magnetic field for a MTJ consisting of TaB buffer/ CoFeB (0.9 nm)/MgO (t_{MgO})/CoFeB (3 nm). Here, the bottom ultrathin CoFeB serves as the perpendicularly-magnetized free layer, whose PMA can be controlled by voltage application. The top CoFeB acts as the in-plane magnetized reference layer. When an in-plane magnetic field, H is applied, the magnetization of the free layer gradually aligns with the field direction, whereas the magnetization of the reference layer remains fixed in the film plane. Therefore, the TMR curve reflects the magnetization process of the free layer along its magnetic hard axis direction. The tunneling conductance, G depends on the relative angle (θ) between the magnetizations of the free and reference layers, *i.e.,* $G(\theta) = G_{90} + (G_{\mathrm{P}}-G_{90})\cos\theta$. Here, G_{90} and G_{P} represent the conductance under orthogonal and parallel magnetization configurations, respectively. The ratio of the in-plane component of the magnetization of the free layer, $M_{\text{in-plane}}$, to its saturation magnetization, M_{S}, is expressed as follows:

$$\frac{M_{in-plane}}{M_S} = \cos\theta = \frac{R_{90} - R(\theta)}{R(\theta)} \frac{R_P}{R_{90} - R_P} \qquad (1),$$

where R_P and R_{90} denote the tunneling resistance in the parallel and orthogonal magnetization configurations, respectively. $R(\theta)$ represents the resistance when the magnetization of the free layer is tilted toward the in-plane direction by an angle θ under the application of H.

The PMA energy, K_{PMA}, of the free layer under each bias voltage (V_{bias}) can be calculated from the $M_{in\text{-}plane}(H)/M_S$ curve using the saturation magnetization value obtained from independent magnetization measurements (see the hatched area in the inset of Fig. 3(b) for the case of V_{bias} = 50 mV).

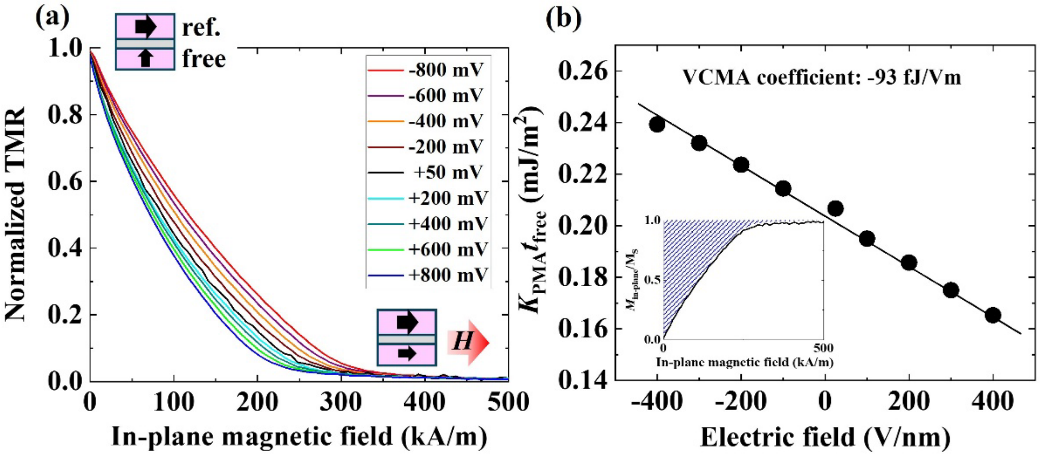

Figure 3 Example of VCMA effect evaluation using an orthogonally magnetized MTJ consisting of TaB/CoFeB (0.9 nm)/MgO/CoFeB (3 nm). (a) Bias voltage dependence of normalized TMR curves measured under in-plane magnetic field application, and (b) applied electric field dependence of $K_{PMA}t_{free}$. The inset shows the normalized M-H curve derived from the TMR curve (V_{bias} = 50 mV). K_{PMA} was calculated from the hatched area.

The evaluated $K_{PMA}t_{free}$ values are plotted as a function of the applied electric field, $E = V_{bias}/t_{MgO}$ in Fig. 3(b). Application of a positive (negative) V_{bias} induces a decrease (increase) in the PMA energy, which is consistent with the trend observed in Fig. 2. In most cases, the $K_{\mathrm{PMA}}t_{\mathrm{free}}$ changes linearly with the applied electric field, and the slope of this relationship is defined as the VCMA coefficient with the unit of J/Vm.

Next, the physical origin of the VCMA effect is briefly described. The magnetic anisotropy energy of ferromagnetic metal can be expressed by the following Laan's equation[29,30].

$$\Delta E_{MA} \approx -\frac{1}{4}\xi\,\widehat{S}\cdot(\langle L_{\downarrow}\rangle - \langle L_{\uparrow}\rangle) + \frac{\xi^{2}}{\Delta E_{ex}}\left(\frac{21}{2}\widehat{S}\cdot\langle T\rangle\right) \qquad (2)$$

Here, ↑ and ↓ represent the majority and minority spin bands, ξ is the spin orbit coupling constant, $\hat{S}$ is the spin magnetic moment, $L_{\uparrow(\downarrow)}$ is the orbital magnetic moment of the majority (minority) spin band, ΔE_{ex} is the exchange splitting energy, and $\hat{S}\cdot\langle T\rangle$ is the magnetic dipole term.

One possible origin of the purely electronic VCMA effect is the electric-field-induced modulation of the orbital magnetic moment in the first term, called the spin-conserving term, which is mediated by carrier-induced changes in the electronic structure at the interface (Fig. 4(a), origin 1)[31-34]. This mechanism can be dominant in strong ferromagnetic materials such as Fe and Co, and is therefore of great practical importance. Another possible origin is the distortion in electron orbits induced by the inhomogeneous electric-field at the metal/dielectric interface. In this effect, the second term of Laan's equation, known as the spin-flipping term[35,36] , also plays an important role. Nonlinear electric fields can induce electric quadrupoles, which in turn can modify magnetic dipoles and thereby change the magnetic anisotropy (Fig. 4(b), origin 2). This mechanism can be dominant in materials with large spin orbit interaction and small exchange splitting energy as indicated in Eq. (2). A representative example is a system in which magnetic moments are induced in nonmagnetic metals, such as Pt in Fe/Pt multilayers, through the proximity effect from adjacent ferromagnetic layers. The inverse VCMA effect, namely the change in charge distribution induced by magnetization oscillations, has also been experimentally demonstrated[37]. Although PMA control utilizing phenomena such as the magneto-ionic effect[38-40] and piezo-electric effect[41] are also interesting approaches due to their large VCMA coefficients exceeding 1000 fJ/Vm, they are not discussed in this paper because their limited writing speed and endurance make them unsuitable for MTJs-based working memory applications, while they may still offer potential for more storage-oriented memory devices.

(a) Origin 1：Modulation in orbital magnetic moment

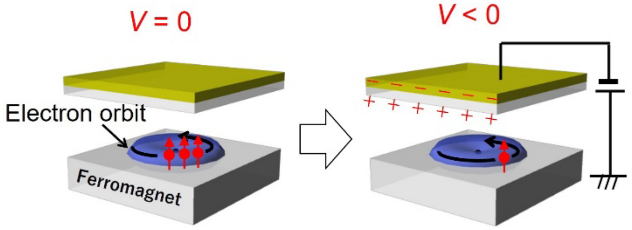

(b) Origin 2：Modulation in electric quadrupole

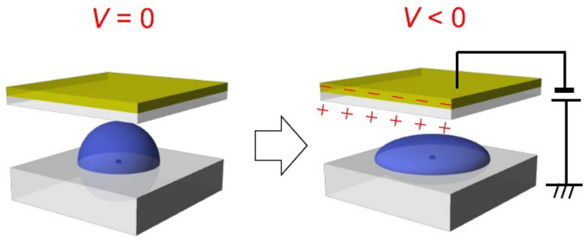

Figure 4 Conceptual diagram of the physical origin of the VCMA effect. Origin 1: carrier-mediated modulation in orbital magnetic moment and Origin 2: inhomogeneous electric-field-indued modulation in electric quadrupole. Origin 1 arises from carrier-mediated modification in the orbital magnetic moment at the interface, which can be dominant in 3*d* transition ferromagnets. In contrast, Origin 2 originates from electric-quadrupole induction caused by inhomogeneous electric fields at metal/insulator interfaces, and provides an important contribution in proximity-induced magnetism with large spin–orbit interaction.

Next, we outline a method for bi-stable magnetization switching utilizing the VCMA effect[42]. As shown in Fig. 2, if the intrinsic PMA (without applied voltage) is properly engineered, the magnetic easy axis can be controlled between out-of-plane and in-plane directions within the modulation rage provided by the VCMA effect. However, static voltage application alone cannot induce the bi-stable switching required for memory writing. Although the VCMA effect has been reported as an assistive mechanism for magnetic-field[43] or STT switching[44,45], there is a strong demand for achieving magnetization switching solely by voltage application. One possible approach is dynamic magnetization switching[42,46-49] enabled by fast spin dynamics induced by VCMA effect[50,51]. Figure 5 illustrates a conceptual diagram of VCMA-induced dynamic magnetization switching. The initial state is an upward magnetized configuration with an in-plane bias magnetic field H_{ex} applied. By applying a high-speed voltage pulse that instantaneously reduces the PMA to zero, the magnetization starts to precess around the H_{ex}. When the pulse voltage is turned off at the moment the magnetization has rotated exactly half a turn, it relaxes to the other energy minimum of the PMA, thereby completing the magnetization switching. If the pulse duration corresponds to a full rotation, the magnetization returns to its initial state, resulting in no apparent switching. Thus, in this magnetization switching scheme, the switching probability exhibits oscillatory behavior depending on the number of magnetization rotations as determined by the pulse duration. Under the long pulse duration, as the magnetization repeatedly rotates and eventually points along the in-plane magnetic field direction, the switching probability finally converges to 0.5. Figure 5(b) shows an example evaluation of the write error rate (WER) as a function of the write pulse duration in voltage-induced dynamic magnetization switching. The WER exhibits oscillatory behavior and increases rapidly with increasing pulse duration. A half-turn precession is optimal for achieving a lowest WER with fast switching, and its pulse duration, t_{SW} is expressed by the following equation.

$$t_{SW} \sim \frac{\pi(1-\alpha^2)}{\gamma\mu_0 H_{ex}} \qquad (3),$$

where α, γ, μ_0 are the magnetic damping constant, the gyromagnetic ratio and the permeability of vacuum, respectively. As the damping constant is typically much smaller than one, the switching time is primarily determined by the amplitude of H_{ex}. To achieve low WER, it is important to realize high PMA, large VCMA effect, and low magnetic damping to suppress the influence of thermal fluctuation[52,53].

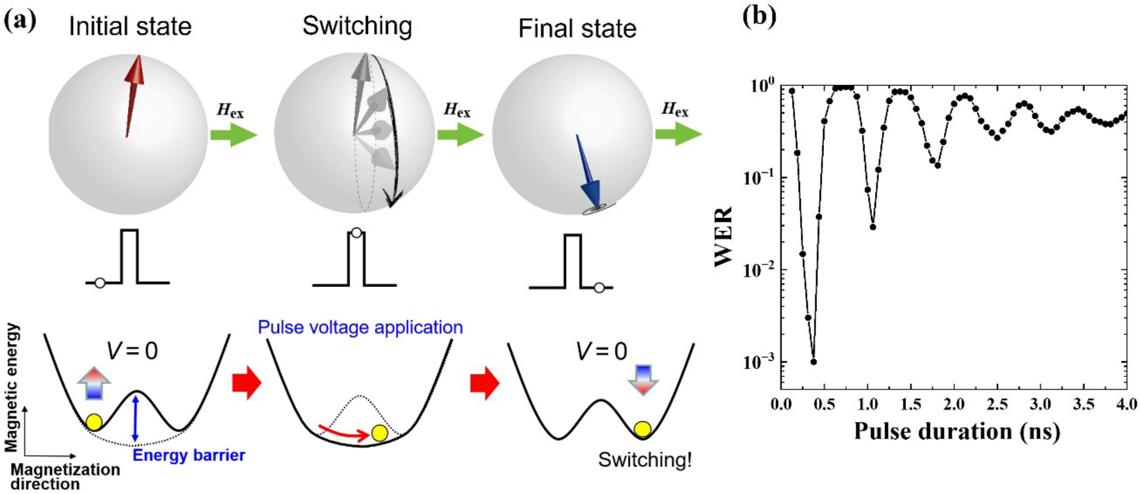

Figure 5 (a) Conceptual illustration of pulse voltage-induced dynamic magnetization switching. Under the application of an in-plane bias magnetic field H_{ex}, a high-speed voltage pulse, which reduces the PMA to zero, induces magnetization precession around H_{ex}. By turning off the pulse voltage at the timing when the magnetization reaches the energy stable point opposite to the initial state, magnetization switching can be realized. (b) Example of the pulse duration dependence of the write error rate in experimentally observed voltage-induced dynamic magnetization switching.

Improvement in these factors have enabled WER values of the order of 10^{-6} in experiments[54,55]. On the other hand, its extreme sensitivity to the pulse duration and the requirement of applying an in-plane magnetic field as the axis of precessional dynamics pose challenges for practical applications, therefore various solutions have been proposed so far[23,56-58]. At present, the VCMA coefficient is not sufficiently high, and therefore a relatively high pulse voltage is required for the dynamic magnetization switching process. Nevertheless, a write endurance on the order of 10^{11} cycles has been demonstrated[20,23,24].

Regarding the read operation, there is a significant difference between STT-MRAM and VC-MRAM, as illustrated conceptually in Fig. 6. In bipolar-switching for STT-MRAM, the read and write currents must be sufficiently separated to avoid read disturb. In contrast, in unipolar-switching for VC-MRAM, the write and read operations can be performed with opposite polarities, allowing read disturb to be fundamentally avoided. Furthermore, in the read-operation polarity, the PMA can be increased due to the VCMA effect; therefore, applying a larger read voltage enhances robustness against read disturb, enabling readout at higher output levels compared to STT-MRAM[59].

Another important technical challenge in the development of VC-MRAM is the enhancement of the VCMA coefficient for demonstrating scalability[20,21]. As mentioned above, dynamic magnetization switching utilizing the VCMA effect requires reducing the PMA to zero by applying a pulse voltage. On the other hand, in order to ensure sufficient thermal stability, Δ, of the magnetic information in the voltage-controlled free layer, a larger PMA is required as the MTJ size decreases.

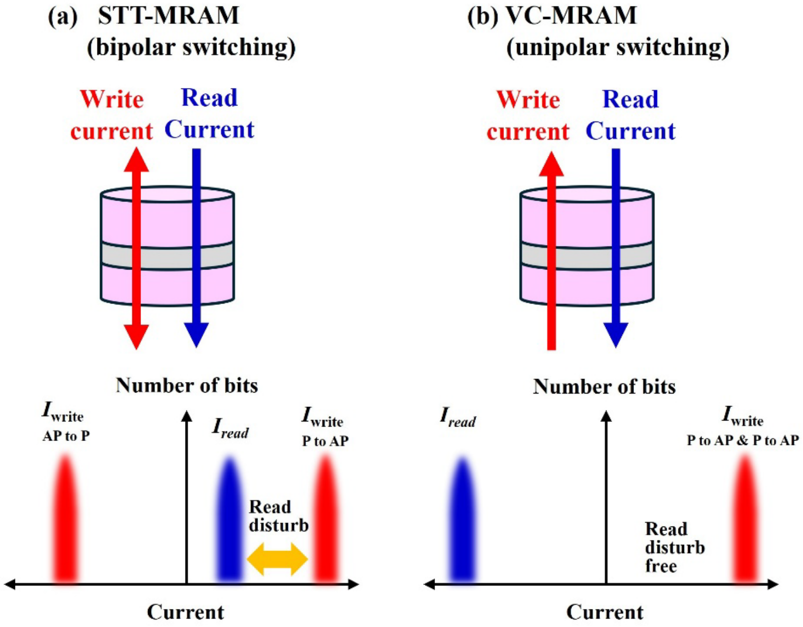

Figure 6 Schematic illustration of the write and read operations in (a) STT-MRAM and (b) VC-MRAM. In bipolar-switching process for STT-MRAM, a sufficient window between the read current and write current must be ensured to avoid read disturb. In contrast, in unipolar-switching VC-MRAM, read disturb can be avoided by performing the read and write operations with opposite polarities.

Figure 7 presents an example of the dependence of the required VCMA coefficient on the MTJ diameter for free layers with each target Δ value. In this estimation, we assume a free layer thickness of 1.5 nm, a tunneling barrier thickness of 1.4 nm, a switching voltage of 1 V, and an operating temperature of 300K. For example, considering an MTJ with a diameter of 40-50 nm, a VCMA coefficient exceeding 300 fJ/Vm is required for short-term retention applications such as temporary buffers in AI chips. On the other hand, for long-term retention applications, such as a memory for learned parameters, these would require a VCMA coefficient exceeding 500 fJ/Vm for ensuring large capacity and high thermal stability. Furthermore, for operation in high-temperature environments, an even larger VCMA coefficient, ideally 1000 fJ/Vm, is demanded.

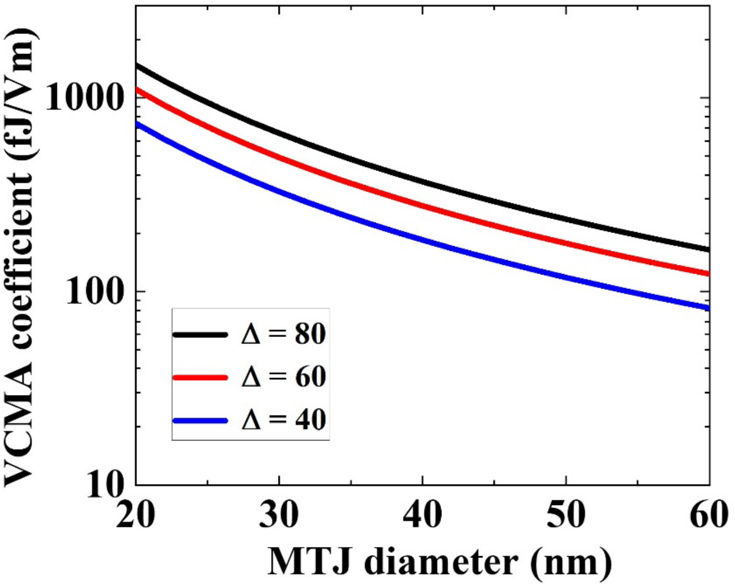

Figure 7 An example estimation of the VCMA coefficient required for magnetization switching of free layers with various thermal stability factors Δ, as a function of MTJ diameter. Here, a free layer thickness of 1.5 nm, a switching voltage of 1 V, a tunneling barrier thickness of 1.4 nm and an operating temperature of 300K were assumed.

The VCMA effect is expected to be applied not only to VC-MRAM but also to various other applications such as voltage-controlled domain-wall devices[60,61], magnonic devices[62], skyrmionic devices[63-67], spin-orbit-torque devices[68], random number generators[69], reservoir computing[70,71], probabilistic computing[72] and quantum computing[73,74]. Therefore, improving the VCMA effect is an important technical challenge that will significantly contribute to the development of electric-field controlled spintronic devices.

3. Fundamental materials studies for improving the VCMA coefficient

This section provides an overview of fundamental materials exploration approaches aimed at improving VCMA effect, mainly through epitaxial MTJs[28,75-83]. As discussed in Fig. 4, the modulation of the orbital magnetic moment due to charge accumulation/depletion is the main origin of the VCMA effect in 3*d* transition ferromagnets. Therefore, the simplest idea for improving the VCMA coefficient is to use a high-k dielectric layer. Fig. 8 presents an example of the VCMA effect evaluation in a Ta/FeB (1.4 nm)/MgO (1.5 nm)/HfO_x (0.95 - 5 nm)/Pt junctions performed by polar MOKE measurements[84]. By varying the HfO_x thickness with fixing the MgO thickness at 1.5 nm, the effective dielectric constant of the entire dielectric layer can be systematically controlled as shown in Fig. 8(a). We confirmed that the VCMA coefficient has a positive correlation with the effective dielectric constant and increases monotonically as expected (Fig. 8(b)).

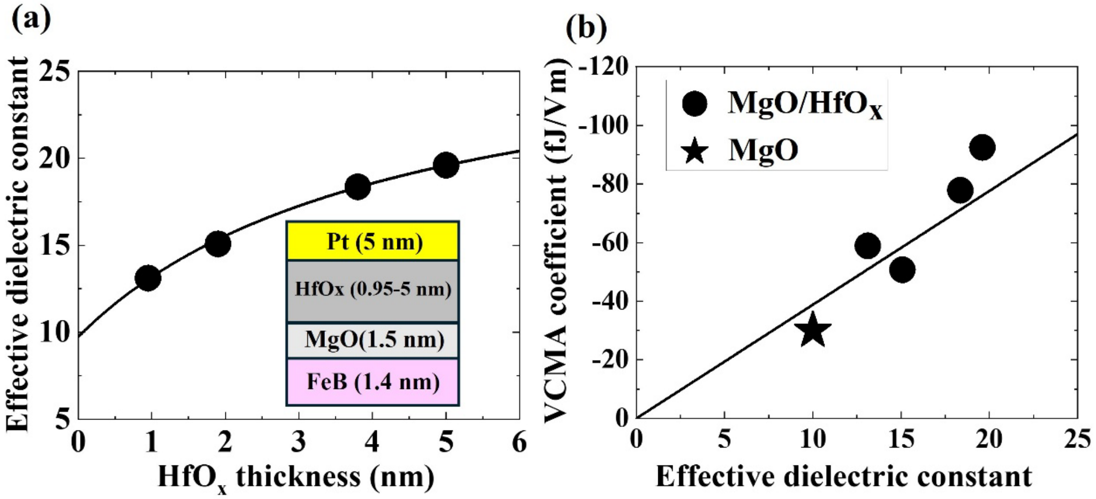

Figure 8 (a) Effective dielectric constant of the MgO (1.5 nm)/HfO_x (0.95-5 nm) bilayer dielectric layer, and (b) effective dielectric constant dependence of VCMA coefficient in FeB/MgO/HfO_x/Pt junctions. Adapted with permission from Ref. [84].

Although the introduction of high-k materials into MTJ devices is challenging from the viewpoint of the coherent TMR effect, the coexistence of the VCMA effect and the TMR effect has been demonstrated in stacked tunneling barrier structures such as MgO/PZT/MgO[85] and MgO/cubic ZrO_2/MgO[77]. However, at present, these structures tend to exhibit lower TMR than a single-layer MgO barrier; therefore, the realization of a crystalline high-k tunnel barrier capable of achieving high-quality coherent tunneling remains an important challenge.

From the viewpoint of materials design for the ultrathin ferromagnetic layer, the introduction of heavy metal materials with proximity-induced magnetism is an important approach, which was first theoretically proposed by Nakamura *et al*[86]. They demonstrated, through first-principles calculations, that inserting a single atomic layer of 5*d* elements such as Ir or Os at the Fe/MgO interface significantly enhances the VCMA effect. In real MTJ devices, it is not easy to realize the insertion of a single atomic layer of heavy metal. Actually, in Cr/Fe/ultrathin Ir/MgO/Fe epitaxial junctions, we found that Ir atoms diffuse into Fe during the deposition and post-annealing processes. Ir diffusion into Fe was confirmed directly by high-angle annular dark field (HAADF) - scanning transmission electron microscopy (STEM) as seen in Fig. 9(a)[75]. Since it is key to reveal the structure-property relationships to accelerate materials and device development, TEM analysis techniques used for MTJ structure evaluation have advanced significantly to date and continued to evolve both in observation and sample preparation[87-89]. Interestingly, it was revealed that the ultrathin Fe layer with dispersed Ir has various advantages. Firstly, first-principles calculations predicted that the insertion of an Ir atomic layer at the Fe/MgO interface prefers strong in-plane magnetic anisotropy, making it difficult to achieve perpendicularly-magnetized free layer. However, it was found that when Ir is dispersed within Fe, it enhances the PMA. As shown in Fig. 9(b), inserting 0.1 nm-thick Ir at the interface of a Fe (1 nm)/MgO junction, which normally exhibits in-plane magnetization, enables perpendicular magnetic easy axis. And the ultrathin Fe layer with dispersed Ir exhibits a large VCMA coefficient. Figure 9(c) shows the dependence of the VCMA coefficient on the CoFe termination layer composition in the epitaxial Cr/Fe (0.5 nm)/Ir (0.06 nm)/Co_xFe_{1-x} (0.1 nm)/MgO/Fe junctions[76,81]. The use of Ir doping with the optimized $Co_{80}Fe_{20}$ termination has led to the achievement of a large VCMA coefficient, reaching a maximum value of -350 fJ/Vm.

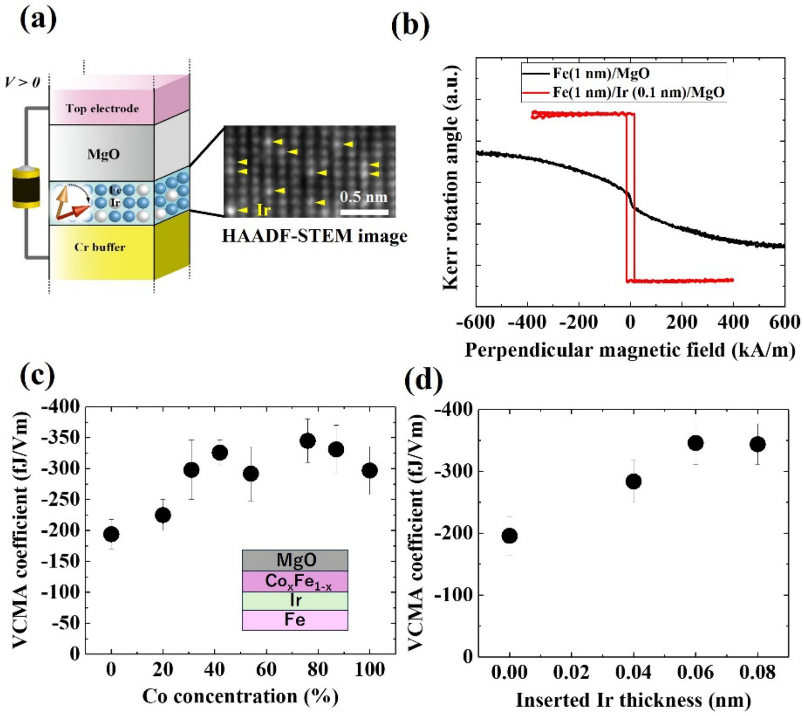

Figure 9 The use of Ir doping technique for highly-efficient VCMA. (a) Schematic illustration of MTJ with an Ir-doped ultrathin Fe free layer and its high angle dark-field scanning transmission electron microscopy (HAADF-STEM) image. (b) Ir doping effect on polar-MOKE hysteresis curves for the ultrathin Fe in Fe(1 nm)/Ir(0 or 0.1 nm)/MgO structure. (c) VCMA coefficient as a function of the Co concentration of the termination CoFe layer in the Cr/Fe (0.5 nm)/Ir (0.05 nm)/Co_xFe_{1-x} (0.1 nm)/MgO/Fe structure. (d) Inserted Ir thickness dependence of VCMA coefficient. Adapted from Ref. [75, 76].

Although Ir doping at the interface generally leads to a reduction in TMR effect, Ir still has the ability to enhance VCMA coefficient even when positioned two atomic layers away from the interface[76]. As a result, it becomes possible to achieve both large VCMA effect and a relatively high TMR ratio simultaneously by inserting a CoFe termination layer. An Ir doping layer thickness of approximately 0.06 nm is sufficient, meaning that a low concentration of doping is already effective, and the VCMA coefficient tends to saturate at higher Ir thicknesses (Fig. 9(d)). This Ir doping technique has also been found to be effective in improving the VCMA effect in polycrystalline MTJs as will be described later. Ir doping can also be achieved by diffusion from a buffer layer[90] or capping layer[91], and in this case, improved annealing tolerance is observed compared to direct doping. Because Ir atoms substitute Fe while maintaining the bcc structure and have a significant effect on property modulation even at extremely low concentrations, PMA and the VCMA coefficient can be improved while preserving surface flatness even in the ultrathin film regime. It is also noteworthy that the large VCMA effect exceeding 300 fJ/Vm achieved by Ir doping has demonstrated high-speed response on the order of several hundred picoseconds, as evidenced by voltage-induced FMR[75]. In addition to Ir, systematic investigations have been conducted on the effects of doping with various heavy metal materials on the VCMA characteristics[92-97].

Figure 10 shows an example of the anisotropy energy changes of spin-conserving and spin-flipping terms in the Fe/HM (1 ML)/MgO structure obtained from first-principles calculations conducted by M. Tsujikawa and M. Shirai, where HM represents a single atomic layer of a heavy metal element[98]. In 5*d* transition heavy metal materials, where a large proximity-induced magnetic moment is induced, large PMA changes can be induced in both spin-conserving and spin-flipping terms. However, it should be noted that for any element, the anisotropy energy changes due to the spin-conserving and spin-flipping terms are nearly equal in magnitude but opposite in sign. This means that the VCMA effect from the spin-conserving and spin-flipping terms cancel each other out, and only their difference (shown as "total" in Fig. 10) is apparently obtained. Therefore, the large VCMA effect expected from the large spin-orbit interaction in these elements is not effectively exploited for most cases. Interestingly, a significant difference is observed only in the case of Ir doping, and this is the key factor leading to the large VCMA effect in this case.

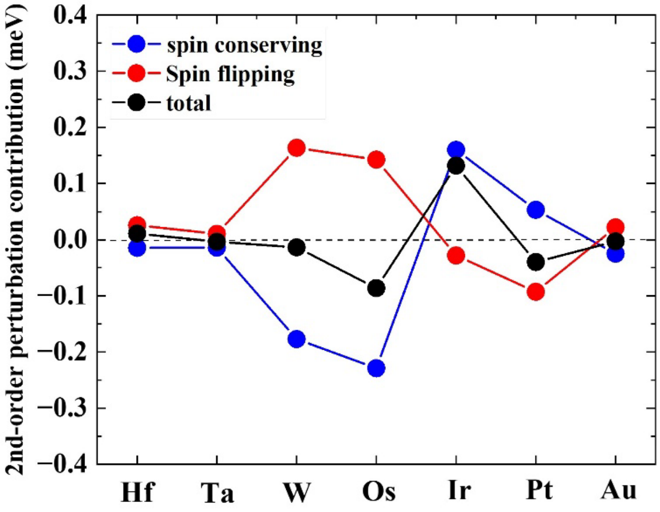

Figure 10 Electric-field-induced anisotropy energy changes of spin-conserving (blue dots), spin-flipping (red dots) terms and sum of them (black dots) in the Fe/HM (1 ML)/MgO structure obtained by first-principles calculations. HM represents a single atomic layer of heavy metal elements of Hf, Ta, W, Os, Ir, Pt and Au.

The interfacial oxidation state is also an important factor in designing structures to exploit the VCMA effect[80,99-102]. Figure 11 presents an example of precise experimental control of the interfacial oxidation state by inserting a naturally oxidized $MgAlO_x$ layer[80]. An ultrathin MgAl layer with a thickness of less than 0.25 nm was formed on a perpendicularly-magnetized Fe/Ir/Co free layer by wedge-shaped deposition. After exposure to a pure oxygen atmosphere at 1×10^{-5} Pa for 3 minutes, an MgO tunneling barrier layer was deposited, followed by a top reference layer with in-plane magnetization. A clear maximum in $K_{\mathrm{PMA}}t_{\mathrm{free}}$ was observed when the MgAl layer thickness was 0.2 nm. The maximum TMR ratio was also observed at the same MgAl thickness. These results suggest that an ideal interfacial oxidation state was achieved under this condition.

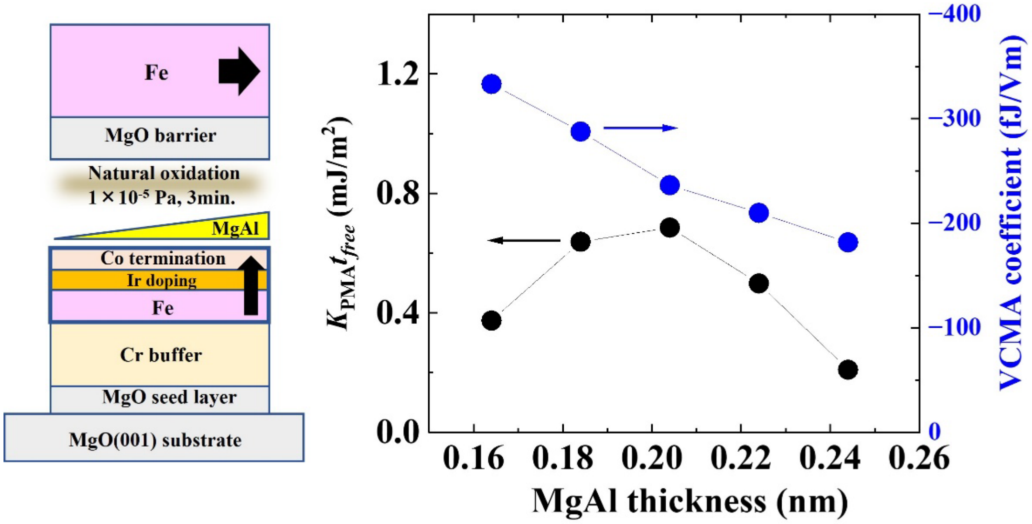

Figure 11 Influence of interfacial oxidation states on VCMA effect. A wedge-shaped MgAl layer was deposited on the Fe/Ir/Co free layer and oxidized in pure O_2 atmosphere of 1×10^{-5} Pa for 3min. Right figure shows inserted MgAl thickness dependence of $K_{\mathrm{PMA}}t_{\mathrm{free}}$ and the VCMA coefficient. Adapted from Ref. [80].

When the thickness was below 0.2 nm, over oxidation of the magnetic layer is considered to have caused the reduction in PMA, whereas when the thickness exceeded 0.2 nm, the presence of unoxidized MgAl likely led to the decrease in PMA. Interestingly, the VCMA coefficient exhibited a completely different dependence on MgAl thickness, showing a tendency to increase monotonically as the MgAl thickness decreased. This indicates that a larger VCMA effect was obtained under the weakly-oxidized condition. Although the origin of the observed trend is not yet clear, Nakamura *et al.* have proposed that when a transition metal oxide monolayer exists at the interface, such as in an Fe/FeO/MgO structure, slight positional shifts of the transition metal atoms induced by the electric field can give rise to an additional enhancement of the VCMA effect[103]. Provided that the response speed is guaranteed, this phenomenon is expected to serve as an effective strategy for enhancing the VCMA coefficient.

Tetragonal distortion in the MgO thin layer also can contribute to the enhancement of the VCMA coefficient[78]. We systematically investigated the thickness dependence of the lattice parameter of nanometer-thick MgO films deposited on epitaxial Cr/Fe, which is commonly used in epitaxial MTJ structures, and found that tetragonal distortion occurs due to compressive stress of about 1.5% (see Fig. 12(a)), resulting in an increase in the dielectric constant to around 15 (compared to the bulk value of 10). The observed distortion induces an increase in the dielectric constant of MgO, leading to the enhancement of VCMA effect as shown in Fig. 12(b). This trend can be regarded as an intermediate stage toward the emergence of ferroelectricity in rock-salt oxides with large tetragonal distortion, as exemplified by results on BaO and EuO[104]. Since the critical strain for MgO to become ferroelectric is around 8%, there is still room for further improvement in the dielectric constant; however, achieving a similar effect in polycrystalline MTJ structures remains a challenge.

As introduced in this section, in epitaxial MTJs, a high VCMA coefficient of the order of 300 fJ/Vm with high-speed response has been achieved through purely electronic VCMA effects by approaches such as the introduction of high-k dielectric layers, heavy element doping, and interfacial oxidation control. However, for practical device applications, the challenge remains to achieve a comparable or even larger VCMA effect in polycrystalline MTJs.

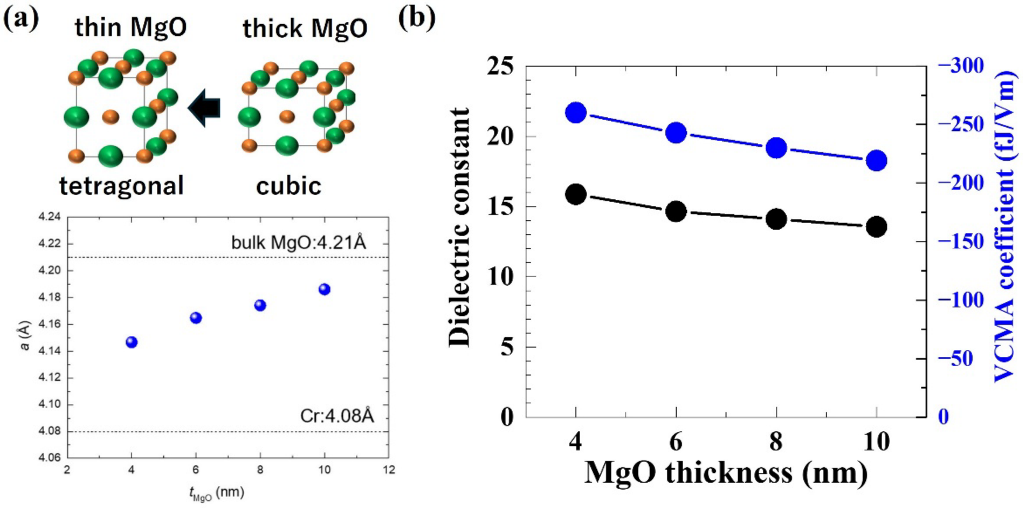

Figure 12 (a) Tetragonal distortion of MgO thin films induced by strain from epitaxial growth. (b) MgO thickness dependence of dielectric constant and VCMA coefficient observed in epitaxial Cr/Fe/Ir/Co/MgO structures. Adapted from Ref. [78].

4. Improvement of the VCMA properties in polycrystalline MTJs

This section describes efforts aimed at improving the VCMA effect in polycrystalline MTJs. In polycrystalline ultrathin multilayer structures prepared by sputtering processes, it is more challenging to control properties such as crystallinity, interface flatness, and interface cleanliness compared to epitaxial ones. These factors are expected to have an even greater impact, since the VCMA effect is highly sensitive to the interfacial condition.

In epitaxial MTJs, it is difficult to form ultrathin magnetic layers, such as a few monolayers of Fe on MgO, and thus most studies have focused on bottom-free-type MTJs in which the free layer is located on a bottom metal buffer layer that ensures higher flatness and higher crystalline quality. In contrast, in polycrystalline MTJs, it is feasible to fabricate amorphous CoFeB layers of about 1 nm thickness with a relatively flat surface even on MgO, and therefore various experimental studies have been conducted using both bottom-free and top-free type MTJ structures.

In this section, we introduce several examples of performance improvement achieved by utilizing cryogenic temperature deposition installed in a mass-production sputtering system (EXIM, Tokyo Electron ltd.). In this system, using a stage cooled by a helium refrigerator and electrostatic chucking during deposition, the substrate can be cooled to below 100 K within less than 20 seconds, and deposition can be performed while rotating the stage, making the system compatible with mass-production processes.

An advantage of the bottom-free type MTJ is that it enables the formation of a flat free layer on a metal buffer material, and in fact, various efforts have been made to enhance the VCMA effect by optimizing the buffer materials[90,105-108]. Figure 13 summarizes an example of VCMA property evaluation for a CoFeB free layer that was optimized through the use of a TaB buffer and a cryogenic temperature deposition process[109]. The cross-sectional bright field (BF)-STEM image (Fig. 13(b)) confirms that a very flat CoFeB layer, even at a thickness of 0.9 nm, is formed on the amorphous metal buffer. Of particular interest is that CoFeB deposited on the TaB buffer at cryogenic temperature; 100K, exhibited larger VCMA coefficient than that deposited at room temperature as shown in Fig. 13(c). Although almost no change in the morphology of CoFeB was observed depending on the deposition temperature, the CoFeB deposited at 100K showed a slightly higher saturation magnetization. This suggests that intermixing at the TaB/CoFeB interface during deposition was suppressed by the cryogenic temperature deposition process. This suppression is also expected to have contributed to the cleanliness of the CoFeB/MgO interface by reducing Ta contamination, thereby improving the VCMA effect. Furthermore, the VCMA coefficient was enhanced to -138 fJ/Vm by adopting a CoFeB(0.8 nm)/Ir(0.05 nm)/CoFe(0.1 nm) stacked free layer (Fig. 13(d)), based on optimizations found in epitaxial MTJs as discussed in Fig. 9(c).

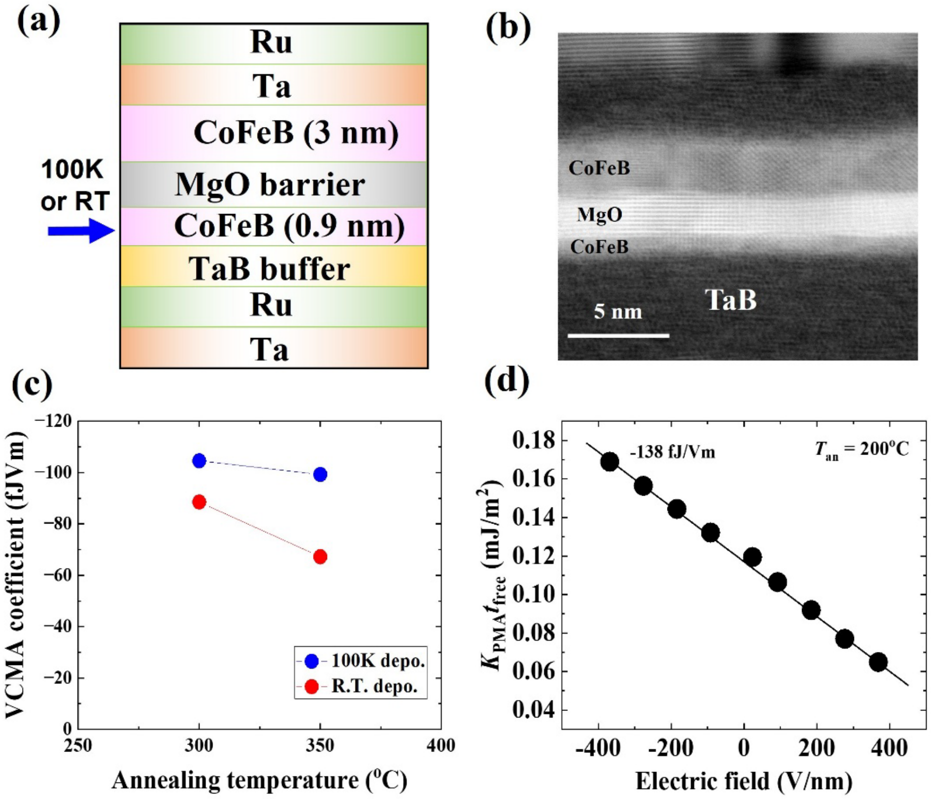

Figure 13 (a) Schematic illustration of the multilayer structure used to examine the effect of cryogenic temperature deposition on bottom-free type MTJs and (b) cross-sectional bright field-STEM image around the MgO tunneling barrier. (c) Annealing temperature dependence of VCMA coefficient observed in the MTJs with CoFeB deposited at 100K (blue dots) and room temperature (red dots.) (d) Optimized VCMA effect obtained in the TaB/CoFeB/Ir/CoFe/MgO/CoFeB structure. Adapted from Ref. [109].

Although Ir doping at the ferromagnet/dielectric interface is effective in improving VCMA effect, it tends to readily disperse into the ultrathin ferromagnetic layer. To address this problem, the use of an ultrathin MgFeO blocking layer was explored as an approach to suppress diffusion during the deposition process[110]. As shown in Fig. 14(a), we prepared an MTJ structure with an ultrathin 0.15 nm-MgFeO layer inserted between the CoFeB free layer and the Ir (0.05 nm)/CoFe (0.1 nm) doping bilayer. The CoFeB and CoFe layers were deposited at 100K. Figure 14(b) and (c) show the bias voltage dependence of the normalized TMR curves and the applied electric field dependence of the $K_{\mathrm{PMA}}t_{\mathrm{free}}$ for this structure. A large VCMA coefficient of -167 fJ/Vm was observed due to the Ir diffusion blocking effect of the MgFeO layer during the deposition.

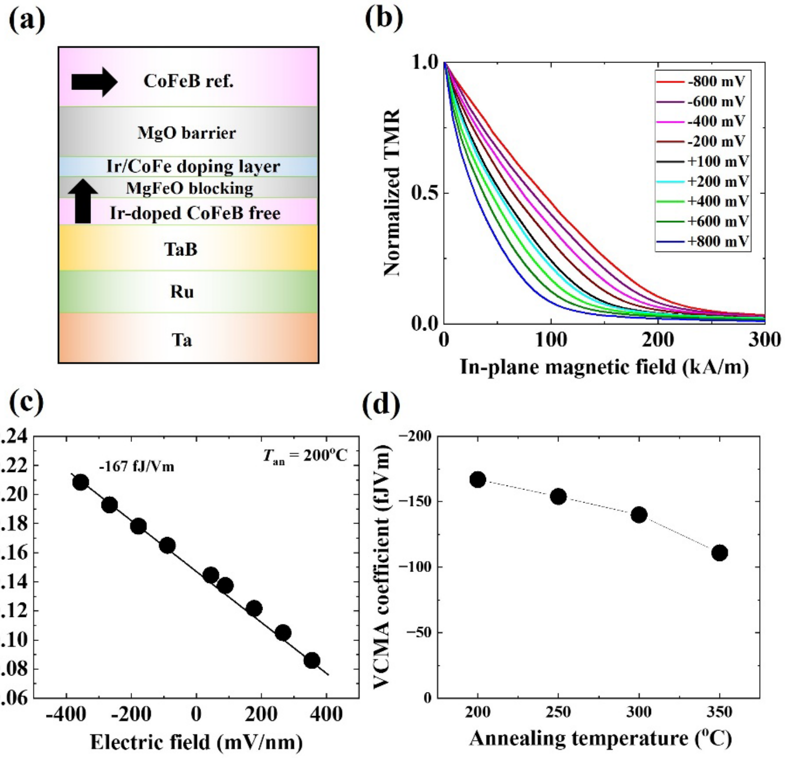

Figure 14 (a) Introduction of the MgFeO blocking layer to suppress the Ir diffusion from the interface. Examples of the (b) bias voltage dependence of normalized TMR curves measured under in-plane magnetic fields and (c) applied electric field dependence of $K_{\mathrm{PMA}}t_{\mathrm{free}}$ obtained in the optimized TaB/Ir-doped CoFeB/MgFeO blocking layer/Ir/CoFe/MgO/CoFeB structure. (d) Annealing temperature dependence of VCMA coefficient. Adapted from Ref. [110].

However, a drawback of this bottom-free type structure is its low annealing tolerance, which mainly arises from interfacial contamination caused by diffusion of the buffer materials during high-temperature annealing. If these issues can be resolved and a high annealing tolerance can be achieved, the large VCMA effect can be effectively utilized in the bottom-free type MTJs. It should be noted, however, that the difficulty of preparing a top-reference layer with robust magnetic properties is also an important technical challenge in bottom-free type MTJs.

In contrast, whilst top-free type MTJs exhibit advantages such as higher annealing tolerance in MgO double barrier structure and better compatibility with high-quality bottom reference layers, they generally show smaller VCMA coefficient compared to bottom-free type structures due to the difficulty in forming high-quality ultrathin magnetic layers on MgO. However, it has been found that cryogenic temperature deposition is also more effective in top-free type MTJs[53,111-113].

Figure 15 presents a study examining how the deposition temperature of CoFeB on MgO influences the TMR, PMA and VCMA properties of orthogonally-magnetized MTJs consisting of Ta/CoFeB (3 nm)/MgO (2 nm)/CoFeB (t_{CFB})/Mo(0.1 nm)/Ta structure[111]. Here, the bottom CoFeB layer serves as the in-plane magnetized reference layer, while the top CoFeB layer acts as the perpendicularly-magnetized free layer whose PMA is controlled by voltage. A comparison of TMR curves measured under an in-plane magnetic field is shown in Fig. 15(a) for CoFeB deposited on MgO at room temperature (red dots) and at 100K (blue dots). The samples were post-annealed at 300°C. By introducing cryogenic temperature deposition, clear improvements in both the TMR ratio and PMA have been observed. Analogous to the bottom-free structure, a slight increase in saturation magnetization was observed, suggesting that the reduction of interfacial mixing at the MgO/CoFeB interface contributed to the improvement of these properties. Cryogenic temperature deposition was also effective in enhancing the VCMA effect, resulting in an approximately twofold improvement (Fig. 15(b)). However, the absolute value remained low at around 50 fJ/Vm, probably due to interfacial contamination caused by diffusion of the Mo cap layer.

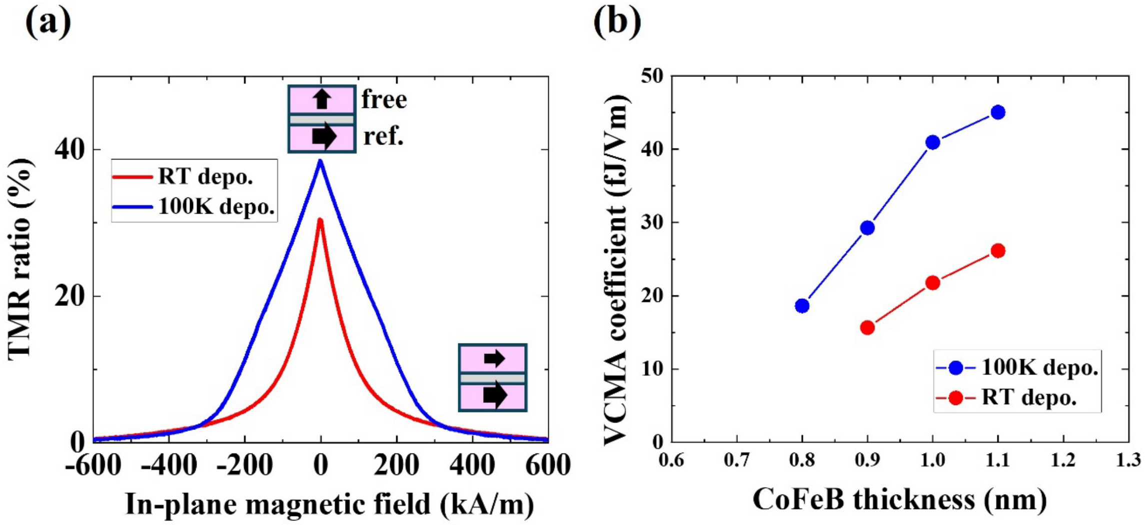

Figure 15 Effect of cryogenic temperature deposition on an ultrathin CoFeB deposited on MgO tunneling barrier. (a) Comparison of TMR curves obtained in the MTJs consisting of Ta buffer/CoFeB/MgO/CoFeB/Mo cap, where an ultrathin CoFeB top free layers were deposited at 100K (blue dots) or room temperature (red dots). (b) CoFeB free layer thickness dependence of VCMA coefficient. Adapted with permission from Ref. [111].

It was recently demonstrated that the introduction of MgO double barrier structure and a boron-less CoFe top-free layer prepared by cryogenic temperature deposition is effective for improving the VCMA effect in top-free type MTJs[113]. When an ultrathin CoFe film is formed on MgO at room temperature, it tends to grow in an island-like manner due to the lower surface energy of MgO compared to that of CoFe. However, when CoFe is deposited at cryogenic temperature, a well-crystallized ultrathin film with (001) orientation is obtained even in the as-deposited state, indicating grain-to-grain epitaxial growth, as shown in Fig. 16(a). The effect of the CoFe layer deposition temperature on the PMA properties in the MgO/CoFe/MgO double barrier structure is displayed in Fig. 16(b). CoFe deposited at room temperature exhibits superparamagnetic behavior, indicative of its island-like growth mode (black dots). In contrast, deposition at 100K yields a well-defined PMA (red dots). Furthermore, the use of an $Mg_{40}Fe_{10}O_{50}$ (hereafter referred to as MgFeO) barrier results in a more pronounced improvement (blue dots). It has been found that the MgFeO tunneling barrier induces Fe segregation at the interface during post-annealing, leading to the formation of a well-defined Fe/MgO interface[114-116]. As a result, improvements such as enhanced interfacial PMA and lower magnetic damping properties can be achieved. In the example shown in Fig. 16(b), the introduction of MgFeO clearly improves the squareness of the hysteresis loop, suggesting an enhancement in PMA. The slight increase in magnetization is attributed to a Fe segregation effect from the MgFeO.

Figure 16(c) summarizes the effect of inserting an Ir doping layer at the MgFeO/CoFe interface on the VCMA coefficient. With optimal Ir insertion of approximately 0.15 nm, a large VCMA coefficient exceeding 100 fJ/Vm is achieved even after post-annealing at 400°C. The developed MTJ with the CoFe top-free layer deposited at 100K exhibited superior voltage-induced dynamic magnetization switching characteristics, as shown in Fig. 16(d). In addition to achieving a low WER of the order of 10^{-6} during a half-turn precession, a WER of the order of 10^{-3} was also obtained even in the relatively long pulse regime of around 1.5 ns. This is attributed to the enhancement in VCMA coefficient and the reduction of magnetic damping. The successful formation of smooth and highly crystalline CoFe in the ultrathin regime through cryogenic temperature deposition holds great potential for providing significant flexibility in the material and structural design of top-free layers. For example, metastable bcc-Co(Fe)Mn is expected as a material that simultaneously achieves low magnetic damping, high PMA, and high TMR[117,118]. We have successfully realized a moderate PMA and a TMR ratio exceeding 100% in an MTJ using this material as a top-free layer, by employing cryogenic temperature deposition and introducing a CoMn/Mo/CoFeB multilayer structure[119].

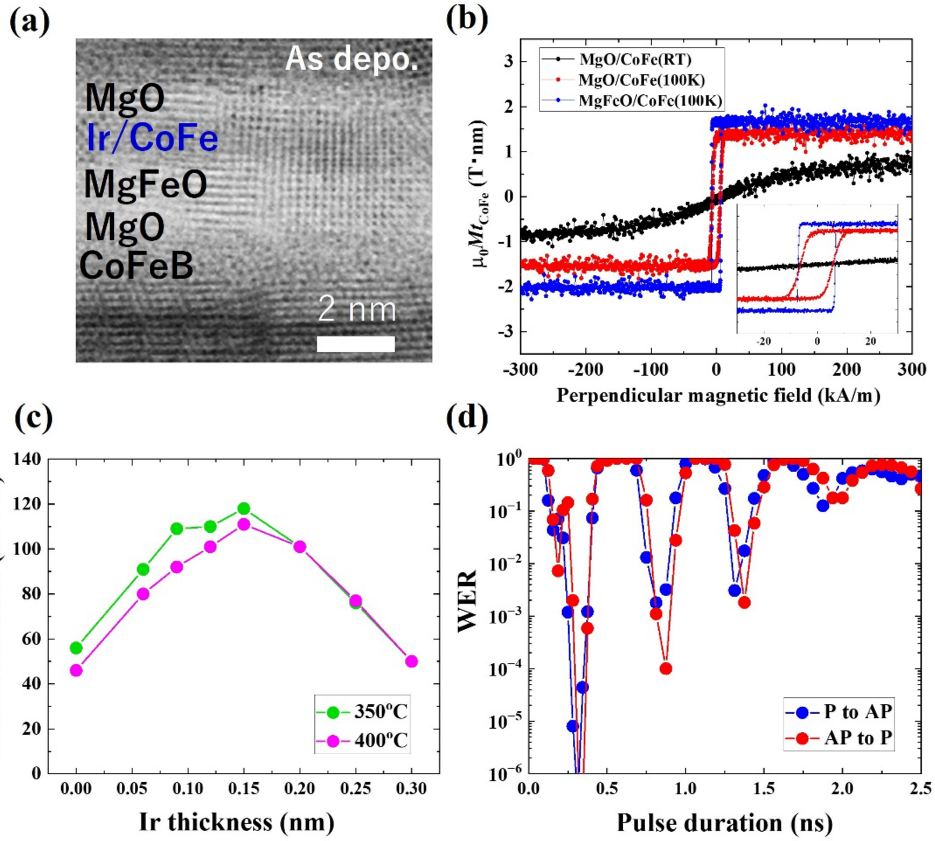

Figure 16 (a) Cross-sectional bright field-STEM image of an ultrathin CoFe deposited on MgFeO tunneling barrier (as deposited state). (b) Comparison of out-of-plane magnetic hysteresis curves for the ultrathin CoFe layer deposited on MgO at room temperature (black dots), CoFe layer deposited on MgO at 100K (red dots) and CoFe layer deposited on MgFeO at 100K (blue dots). (c) Inserted Ir thickness dependence of VCMA coefficient in CoFeB/MgO/MgFeO/Ir/CoFe/MgO structure and (d) example of the pulse duration dependence of write error rate of voltage-induced dynamic magnetization switching. Adapted from Ref. [55].

Cryogenic temperature deposition is expected to be a promising approach for incorporating various materials systems, such as Heusler alloys, $L1_0$-ordered alloys, and tetragonally-distorted alloys, whose integration has been challenging with conventional mass-production sputtering techniques based on room temperature deposition.

For the VCMA effect in polycrystalline structures, the introduction of a cryogenic temperature deposition process has proven highly effective and a large VCMA coefficient of about -170 fJ/Vm has been achieved in MTJs prepared using mass-production sputtering systems. However, further improvement by a factor of 2 to 3 is still desirable. Cryogenic temperature deposition is also expected to open new possibilities for exploring crystalline novel materials, including metastable phases, and to serve as an effective approach for further improving their properties.

From practical perspective, the control of temperature dependence is also a critical factor. Alzate *et al.* reported that although both PMA and VCMA coefficient obey a power-law dependence on saturation magnetization, the VCMA effect exhibits a stronger temperature dependence, suggesting that only specific components of the PMA are sensitive to the electric field[120]. Moreover, controlling magnetic damping is of critical importance for stable magnetization switching as discussed in section 2. While achieving low magnetic damping is regarded as essential for reducing write error rate in dynamic magnetization switching[52], clear experimental validation has not yet been reported. Heavy-metal doping, such as Ir, offers a promising route to improve VCMA coefficient, however it generally increases magnetic damping, highlighting the strong need for strategies that can avoid this issue. In addition, an intriguing topic is the electric-field control of magnetic damping itself, which has also been discussed[121-124]. Needless to say, realizing high endurance in conjunction with meeting these requirements remains an important challenge.

Finally, for reference, Table 1 summarizes representative reports on VCMA coefficient for both epitaxial and polycrystalline MTJs.

Table1 Reported examples of VCMA performance in epitaxial and polycrystalline MTJs

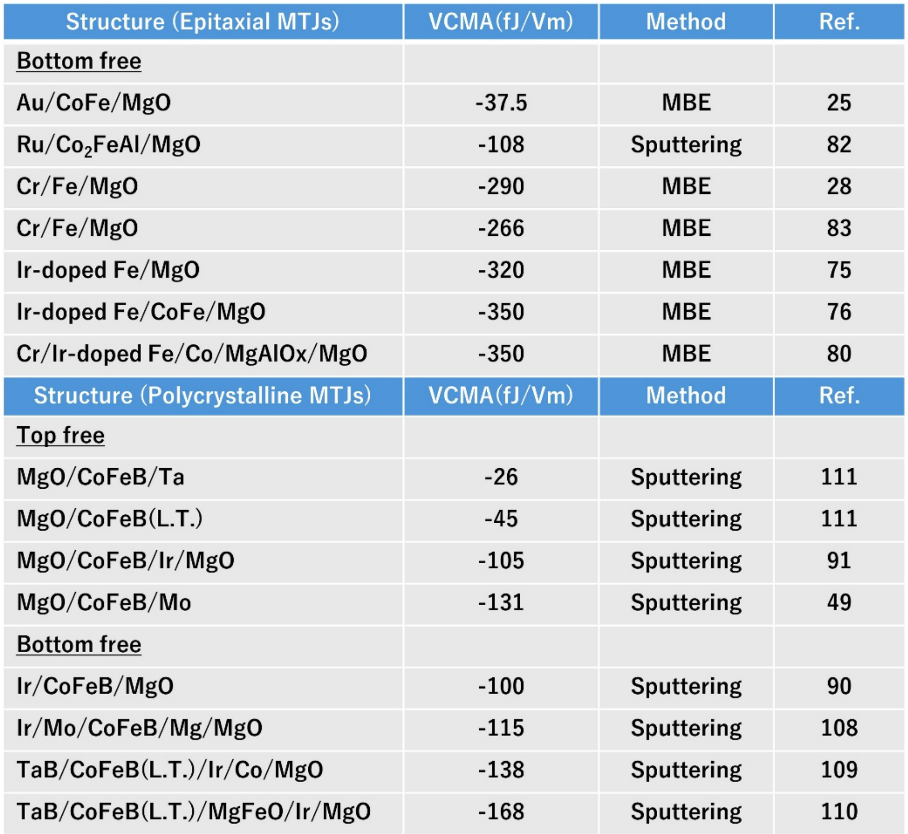

Structure (Epitaxial MTJs)	VCMA(fJ/Vm)	Method	Ref.
Bottom free			
Au/CoFe/MgO	-37.5	MBE	25
Ru/Co$_2$FeAl/MgO	-108	Sputtering	82
Cr/Fe/MgO	-290	MBE	28
Cr/Fe/MgO	-266	MBE	83
Ir-doped Fe/MgO	-320	MBE	75
Ir-doped Fe/CoFe/MgO	-350	MBE	76
Cr/Ir-doped Fe/Co/MgAlOx/MgO	-350	MBE	80
Structure (Polycrystalline MTJs)	**VCMA(fJ/Vm)**	**Method**	**Ref.**
Top free			
MgO/CoFeB/Ta	-26	Sputtering	111
MgO/CoFeB(L.T.)	-45	Sputtering	111
MgO/CoFeB/Ir/MgO	-105	Sputtering	91
MgO/CoFeB/Mo	-131	Sputtering	49
Bottom free			
Ir/CoFeB/MgO	-100	Sputtering	90
Ir/Mo/CoFeB/Mg/MgO	-115	Sputtering	108
TaB/CoFeB(L.T.)/Ir/Co/MgO	-138	Sputtering	109
TaB/CoFeB(L.T.)/MgFeO/Ir/MgO	-168	Sputtering	110

5. Conclusions

A major reason that the VCMA effect has opened a new avenue for voltage-controlled spintronics is that it has enabled electric-field control in commonly used ferromagnetic materials, namely 3*d* transition metals, and made it possible to apply this effect into practically important

MTJ structures. The VCMA coefficient in MTJs has been enhanced to approximately -300 fJ/Vm for epitaxial MTJs and -170 fJ/Vm for polycrystalline devices by employing material design strategies such as heavy metal doping, the integration of high-k dielectric layers, the precise control of the interfacial oxidation states and the use of cryogenic temperature deposition techniques. The VCMA effect is being implemented not only in VC-MRAM but also in a wide range of spintronic devices, such as SOT and skyrmionic devices. These devices require multilayer structures with efficient charge-to-spin conversion channels and strong interfacial DMI, and achieving large VCMA coefficient while maintaining these properties remains a challenging issue. If a highly efficient voltage-driven spin control technology that addresses these challenges can be realized, it would offer an effective approach to reducing the driving energy of various spintronic devices currently controlled by electric current, thereby offering new functional value.

In addition to materials development, ensuring the stability of the write and read operations remains an important challenge toward the realization of VC-MRAM. Unipolar switching in VC-MRAM can avoid the read disturb issue inherent to STT-MRAM by separating the voltage polarities for write and read operations. Moreover, voltage-controlled MTJs employing a thicker tunneling barrier can potentially provide several benefits compared to current-based operation, such as superior write endurance and increased breakdown voltage. However, the dynamic switching process exhibits a higher write error rate compared to deterministic spin-torque switching, and reducing this error remains a major challenge. Approaches such as achieving larger VCMA coefficient and lower magnetic damping are considered essential to address this problem. And also, it is strongly desired to develop techniques that make the switching less sensitive to pulse duration and enable the introduction of an effective bias magnetic field within the device.

If these challenges can be overcome, voltage-driven spintronic technologies—including VC-MRAM—are expected to play a key role in achieving ultralow-power operation in emerging applications such as artificial intelligence (AI) hardware and the Internet of Things (IoT), thereby contributing significantly to future energy-efficient information technology.

Acknowledgements

This work was partly based on results obtained from a project, JPNP16007, commissioned by the New Energy and Industrial Technology Development Organization (NEDO), Japan. A part of TEM analyses were performed with the support of the Foundation for Promotion of Material Science and Technology of Japan (MST). H.N. is supported by the Japan Science and Technology Agency (JST), PRESTO Grant No. JPMJPR23H6.

The authors thank Y. Suzuki of Osaka University (Current affiliation: National Institute of Information and Communications Technology), S. Miwa of the University of Tokyo, Y. Shiota of Kyoto University, H. Kubota, S. Tamaru, H. Onoda (Current affiliation: TDK corporation), T. Ochiai, J. Kim, T. Scheike, S. Tsunegi, T. Taniguchi, Y. Kitaoka, R. Matsumoto, T. Yamaji, H. Arai, A. Fukushima ((Current affiliation: The University of Tokyo)) and H. Imamura of National Institute of Advanced Industrial Science and Technology, L. Sakai, K. Ohba, Y. Higo, and M. Hosomi of Sony semiconductor solutions corporation, S. Mitani, H. Sukegawa and K. Hono of National Institute for Materials Science, M. Shirai, M. Tsujikawa and M. Sahashi of Tohoku University, K. Nakamura of Mie University, T. Oda of Kanazawa University, Y. Miura of Kyoto Institute of Technology for their fruitful discussions.

Conflict of Interest

The authors declare no competing financial interest.

References

[1] D. Worledge *et al.*, *Nat. Rev. Elec. Eng.* **1** 730 (2024).
[2] S. Yuasa *et al.*, *Nat. Mater.* **3** 868 (2004).
[3] S. S. P. Parkin *et al.*, *Nat. Mater.* **3** 862 (2004).
[4] J. C. Slonczewski, *J. Magn. Magn. Mater.* **159** L1 (1996).
[5] L. Berger, *Phys. Rev. B* **54** 9353 (1996).
[6] E. B. Myers *et al.*, *Science* **285** 867 (1999).
[7] J. A. Katine *et al.*, *Phys. Rev. Lett.* **84** 3149 (2000).
[8] C. Safranski *et al.*, in *2022 IEEE Symp. VLSI Technology and Circuits doi:10.1109/VLISTechnologyandCir46769.2022.9830306.* (2022).
[9] F. Matsukura *et al.*, *Nat Nanotechnol* **10** 209 (2015).
[10] H. Ohno *et al.*, *Nature* **408** 944 (2000).
[11] V. Novosad *et al.*, *J. Appl. Phys.* **87** 6400 (2000).
[12] T. Ashida *et al.*, *Appl. Phys. Lett.* **104** 152409 (2014).
[13] K. Toyoki *et al.*, *Appl. Phys. Lett.* **106** 162404 (2015).
[14] L. Gerhard *et al.*, *Nat. Nanotechnol.* **5** 792 (2010).
[15] T. Kimura *et al.*, *Nature* **426** 55 (2003).
[16] J. Wang *et al.*, *SCIENCE* **299** 1719 (2003).
[17] C. G. Duan *et al.*, *Phys Rev Lett* **97** 047201 (2006).
[18] M. Weisheit *et al.*, *Science* **315** 349 (2007).
[19] T. Maruyama *et al.*, *Nat. Nanotechnol.* **4** 158 (2009).
[20] P. K. Amiri *et al.*, *IEEE Trans. Magn.* **51** 3401507 (2015).
[21] T. Nozaki *et al.*, *Micromachines* **10** 327 (2019).
[22] H. Noguchi *et al.*, *IEDM Tech. Dig.* doi:10.1109/IEDM.2016.7838494. (2016).
[23] C.Y. Wu *et al.*, *IEEE Symp. VLSI Tech.* doi:10.1109/VLSITechnology18217.2020.9265057 (2020).
[24] H. Suhail, *IEDM Tech. Dig.* doi:10.1109/IEDM45741.2023.10413670. (2023).
[25] T. Nozaki *et al.*, *Appl. Phy. Lett.* **96** 022506 (2010).
[26] Y. Shiota *et al.*, *Appl. Phys. Exp.* **2** 063001 (2009).
[27] Y. Shiota *et al.*, *Appl. Phys. Exp.* **4** 043005 (2011).
[28] T. Nozaki *et al.*, *Phys. Rev. Appl.* **5** 044006 (2016).
[29] G. van der Laan, *J. Phys. Cond. Mater.* **10** 3239 (1997).
[30] Y. Suzuki *et al.*, *Physics Letters A* **383** 1203 (2019).
[31] C. G. Duan *et al.*, *Phys. Rev. Lett.* **101** 137201 (2008).
[32] K. Nakamura *et al.*, *Phys. Rev. Lett.* **102** 187201 (2009).
[33] M. Tsujikawa *et al.*, *Phys. Rev. Lett.* **102** 247203 (2009).
[34] T. Kawabe *et al.*, *Phy. Rev. B* **96** 220412(R) (2017).
[35] S. Miwa *et al.*, *Nat. Commun.* **8** 15848 (2017).
[36] S. Miwa *et al.*, *J. Phys. D: Appl. Phys.* **52** 063001 (2019).
[37] A. S. Shukla *et al.*, *Sci. Adv.* **6** eabc2618 (2020).

[38] U. Bauer *et al.*, *Nat. Mater.* **14** 174 (2015).
[39] C. Bi *et al.*, *Phys. Rev. Lett.* **113** 267202 (2014).
[40] A. J. Tan *et al.*, *Nat. Mater.* **18** 35 (2019).
[41] G. Yu *et al.*, *Applied Physics Letters* **106** 072402 (2015).
[42] Y. Shiota *et al.*, *Nat. Mater.* **11** 39 (2012).
[43] T. Nozaki *et al.*, *Appl. Phys. Exp.* **7** 073002 (2014).
[44] W. G. Wang *et al.*, *Nat. Mater.* **11** 64 (2012).
[45] S. Kanai *et al.*, *Appl. Phys. Lett.* **104** 212406 (2014).
[46] S. Kanai *et al.*, *Appl. Phys. Lett.* **101** 122403 (2012).
[47] C. Grezes *et al.*, *Appl. Phys. Lett.* **108** 012403 (2016).
[48] T. Yamamoto *et al.*, *J. Magn. and Magn. Mater.* **560** 169637 (2022).
[49] Y. Shao *et al.*, *Commun. Mater.* **3** 87 (2022).
[50] T. Nozaki *et al.*, *Nat. Phys.* **8** 491 (2012).
[51] J. Zhu *et al.*, *Phys. Rev. Lett.* **108** 197203 (2012).
[52] Y. Shiota *et al.*, *Appl. Phys. Exp.* **9** 013001 (2016).
[53] T. Yamamoto *et al.*, *Physical Review Applied* **21** 054008 (2024).
[54] T. Yamamoto *et al.*, *J. Phys. D: Appl. Phys.* **52** 164001 (2019).
[55] T. Ichinose *et al.*, *NPG Asia Mater.* **17.41** (2025).
[56] R. Matsumoto *et al.*, *Phys. Rev. Appl.* **9** 014026 (2018).
[57] R. Matsumoto *et al.*, *Appl. Phys. Exp.* **12** 053003 (2019).
[58] L. Sakai *et al.*, *Applied Physics Letters* **126** 022401 (2025).
[59] C. Grezes *et al.*, *IEEE Magn. Lett.* **8** 3102705 (2016).
[60] D. Chiba *et al.*, *Nat. Commun.* **3** 888 (2012).
[61] A. J. Schellekens *et al.*, *Nat. Commun.* **3** 847 (2012).
[62] B. Rana *et al.*, *Commun. Phys.* **2** 90 (2019).
[63] X. Zhang *et al.*, *Sci. Rep.* **5** 11369 (2015).
[64] T. Nozaki *et al.*, *Appl. Phys. Lett.* **114** 012402 (2019).
[65] M. Schott *et al.*, *Nano Lett.* **17** 3006 (2017).
[66] X. Wang *et al.*, *Nanoscale* **10** 733 (2018).
[67] R. Ishikawa *et al.*, *Appl. Phys. Lett.* **119** 072402 (2021).
[68] H. Yoda *et al.*, *IEDM Tech. Dig.* doi:10.1109/IEDM.2016.7838495 (2016).
[69] A. Fukushima *et al.*, *APL Materials* **9** 030905 (2021).
[70] H. Nomura *et al.*, *Jpn. J. Appl. Phys.* **58** 070901 (2019).
[71] T. Taniguchi *et al.*, *Sci. Rep.* **12** 10627 (2022).
[72] Y. Shao *et al.*, *Nanotechnology* **34** 495203 (2023).
[73] G. Q. Yan *et al.*, *Phys. Rev. Appl.* **18** 064031 (2022).
[74] M. Niknam *et al.*, *Commun. Phys.* **5** 284 (2022).
[75] T. Nozaki *et al.*, *NPG Asia Mater.* **9** e451 (2017).
[76] T. Nozaki *et al.*, *APL Mater.* **8** 011108 (2020).
[77] H. Onoda *et al.*, *Appl. Phys. Exp.* **17** 023001 (2024).
[78] T. Nozaki *et al.*, *NPG Asia Materials* **17.4** (2025).
[79] A. Koziol-Rachwal *et al.*, *Sci. Rep.* **7** 5993 (2017).
[80] T. Nozaki *et al.*, *APL Mater.* **10** 081103 (2022).
[81] T. Nozaki *et al.*, *Appl. Phys. Lett.* **121** 172401 (2022).
[82] Z. Wen *et al.*, *Sci. Rep.* **7** 45026 (2017).
[83] Q. Xiang *et al.*, *J. Phys. D: Appl. Phys.* **50** 40LT04 (2017).

[84] H. Onoda *et al.*, *Phys. Rev. Mater.* **6** 104406 (2022).
[85] D. Chien *et al.*, *Appl. Phys. Lett.* **108** 112402 (2016).
[86] K. Nakamura *et al.*, *J. Magn. Magn. Mater.* **429** 214 (2017).
[87] K. W. Urban, *Science* **321** 506 (2008).
[88] J. Uzuhashi *et al.*, *Ultramicroscopy* **262** 113980 (2024).
[89] J. Uzuhashi *et al.*, *Microscopy* **74** 279 (2025).
[90] W. Skowroński *et al.*, *Appl. Phys. Exp.* **8** 053003 (2015).
[91] T. Nozaki *et al.*, *APL Mater.* **12** 091109 (2024).
[92] T. Bonaedy *et al.*, *Journal of Physics D: Applied Physics* **48** 225002 (2015).
[93] H. Nakayama *et al.*, *Adv. Mater. Interfaces* **10** 2300131 (2023).
[94] D. Lyu *et al.*, *Applied Physics Letters* **124** 182401 (2024).
[95] T. Nozaki *et al.*, *APL Mater.* **6** 026101 (2018).
[96] Y. Hibino *et al.*, *Appl. Phys. Lett.* **109** 082403 (2016).
[97] H. Nakayama *et al.*, *Appl. Phys. Lett.* **122** 032403 (2023).
[98] T. Nozaki, *Mag. Jpn.* **19** 107 (2024).
[99] X. Li *et al.*, *Appl. Phys. Lett.* **110** 052401 (2017).
[100] T. Hirai *et al.*, *Appl. Phys. Lett.* **112** 122408 (2018).
[101] T. Nozaki *et al.*, *Sci Rep* **11** 21448 (2021).
[102] H. Nakayama *et al.*, *APL Mater.* **12** 091122 (2024).
[103] K. Nakamura *et al.*, *Phys. Rev. B* **81** 220409(R) (2010).
[104] E. Bousquet *et al.*, *Phys Rev Lett* **104** 037601 (2010).
[105] W. Skowroński *et al.*, *Phys. Rev. B* **91** 184410 (2015).
[106] T. Yamamoto *et al.*, *Acta Mater.* **216** 117097 (2021).
[107] X. Li *et al.*, *Appl. Phys. Lett.* **107** 142403 (2015).
[108] X. Li *et al.*, *Nano Lett.* **19** 8621 (2019).
[109] T. Nozaki *et al.*, *APL Mater.* **11** 121106 (2023).
[110] T. Nozaki *et al.*, *APL Mater.* **13** 101102 (2025).
[111] T. Ichinose *et al.*, *ACS Appl. Electron. Mater.* **5** 2178 (2023).
[112] A. Sugihara *et al.*, *Appl. Phys. Exp.* **16** 023003 (2023).
[113] T. Ichinose *et al.*, *arXiv:* 2504.07350 (2025).
[114] K. Yakushiji *et al.*, *AIP Advances* **8** 055905 (2018).
[115] T. Ichinose *et al.*, *Applied Physics Express* **16** 113002 (2023).
[116] T. Yamamoto *et al.*, *Acta Materialia* **267** 119749 (2024).
[117] K. Kunimatsu *et al.*, *Japanese Journal of Applied Physics* **58** 080908 (2019).
[118] T. Ichinose *et al.*, *Journal of Alloys and Compounds* **960** 170750 (2023).
[119] T. Yamamoto *et al.*, *Physical Review Applied* **19** 024020 (2023).
[120] J. G. Alzate *et al.*, *Appl. Phys. Lett.* **104** 112410 (2014).
[121] A. Okada *et al.*, *Appl. Phys. Lett.* **105** 052415 (2014).
[122] L. Chen *et al.*, *Phys. Rev. Lett.* **115** 057204 (2015).
[123] B. Rana *et al.*, *Phys. Rev. Appl.* **14** 014037 (2020).
[124] A. Sakoguchi *et al.*, *IEEE Trans. Magn.* **58** 4200105 (2022).